

**THE REVERSIBILITY OF THE ADSORPTION OF METHANE-METHYL
MERCAPTAN MIXTURES IN NANOPOROUS CARBON**

A Thesis presented to
the Faculty of the Graduate School
University of Missouri

In Partial Fulfillment
of the Requirements for the Degree
Master of Physics

by

MONIKA R. GOŁĘBIOWSKA

Dr. Carlos Wexler, Thesis Supervisor

MAY 2011

The undersigned, appointed by the Dean of the Graduate School, have examined the thesis entitled

**THE REVERSIBILITY OF THE ADSORPTION OF METHANE-METHYL
MERCAPTAN MIXTURES IN NANOPOROUS CARBON**

presented by Monika R. Gołębiewska

a candidate for the degree of Master of Physics, and hereby certify that in their opinion it is worthy of acceptance.

Dr. Carlos Wexler, Thesis Supervisor
Department of Physics and Astronomy,
University of Missouri, Columbia

Dr. Peter Pfeifer
Department of Physics and Astronomy,
University of Missouri, Columbia

Dr. Michael Roth
Department of Physics,
University of Northern Iowa, Cedar Falls

ACKNOWLEDGEMENTS

First, I would like to thank Carlos Wexler for enlightening discussions and lots of ideas. His advice and contribution to my work have been very important. I would like to thank him for allowing me to develop the kind of confidence and character traits which will allow me to pursue a successful research career.

Second, I would like to thank Michael Roth who has always been available for help and strongly contributed to my understanding of Molecular Dynamics simulations. I am grateful for his patience and continuous involvement.

I would like to thank Lucyna Firlej and Bogdan Kuchta for their support throughout the duration of the project. They strongly contributed to my intellectual upbringing in physics.

I would like to express my gratitude to Peter Pfeifer. His kindness and support have been invaluable through the course of my apprenticeship.

The project was supported by Grant Number 500-08-022 from California Energy Commission.

I have also been fortunate to be surrounded by colleagues and friends from ALL-CRAFT group. I have benefited immensely from their knowledge throughout discussions and collaborations on various research projects, and from the friendship which sustained me throughout the years. Special thanks to Raina Olsen for companionship and assistance in all aspects of life.

Some people come into our lives and quickly go. Some stay for awhile and leave footprints... Thus, I would like to thank all the others I have met and who influenced me because without them I might not be here.

Last but not least, I would like to thank my mother for her love, understanding and her continual support in pursuing my dreams. She encouraged me to take the road which led to where I am now. Dziękuję Ci, Mamo.

Contents

List of Figures	iv
List of Tables	vi
1. Introduction	1
2. Simulation method: Molecular Dynamics	5
2.1. Initialization	6
2.2. Force calculations	7
2.3. Verlet algorithm.....	8
2.5. Periodic boundary conditions.....	9
3. Simulation setup	11
4. Choice of force field	14
5. Results and discussion	24
5.1. Adsorption isotherms	24
5.2. Adsorption energy: maximum value and fluctuations, mobility	26
5.3. Diffusion in adsorbed methane-methyl mercaptan mixtures.....	30
5.3.1. Graphene surface.....	30
5.3.2. 0.7 nm slit-shaped pores.....	32
5.4. Required enhancement of mercaptan concentration in natural gas	38
6. Summary and Conclusions.....	41
References	43

List of Figures

Figure 1. Methane storage capacity per liter of adsorbent as a function of pressure. At pressure equal 3.5 MPa nearly 100 g of natural gas can be stored in a tank filled with adsorbent such as activated carbon. The same amount of condensed natural gas (CNG) can be stored in an empty tank at pressure about 17 MPa.	2
Figure 2. Nanoporous material for vehicular applications-from corn cob to monolith in tank. [18].....	3
Figure 3. Two-dimensional periodic domain showing unit cell (in the center of the scheme) and its images (surrounding replicas).	10
Figure 4. Side view of the $14.0 \times 10.0 \times 21.0 \text{ nm}^3$ simulation box containing three graphene sheets (blue circles), methane (small green circles) and methyl mercaptan (larger, blue and yellow circles). The graphene sheets are $10.0 \times 10.0 \text{ nm}^2$, leaving space for a gas phase in equilibrium with the adsorbed phase. a) the initial placement of gas molecules beyond slit volume. b) Stabilized system. Periodic boundary conditions were used in all directions.	12
Figure 5. a) Gas distribution on the edge of a typical slit. b) Corresponding density profile of molecules in x-direction (outside the slit, $x < 2 \text{ nm}$).	13
Figure 6. OPLS-UA representation of methane (left) and methyl mercaptan (right).	16
Figure 7. a) All Atom representation of methane: tripod down, tripod up and United Atom molecule, b) Comparison of the interaction energies between three representations.....	18
Figure 8. Comparison of methane-graphite interaction energy calculated using OPLS parameters with selected data available in literature: a) AA approach, b) UA approach.	20
Figure 9. Energy of methane interaction with 1, 2, 3, and 4 layers of graphene: a) UA representation of methane, b) AA representation of methane (tripod down configuration).	22
Figure 10. Snapshots of methyl mercaptan-methane mixture at 195 K (below its boiling point) and molar fractions of CH ₃ SH equal a) 0.065, b) 0.019. Aggregation of mercaptans at the higher concentration is seen. For clarity only CH ₃ SH molecules are shown.....	23
Figure 11. Adsorption isotherms of methane-mercaptan mixtures in 0.7 nm slits at a) 195 K, b) 298 K, c) 320K.	25

Figure 12. Graphene-methane interaction energy vs. time step for various representative molecules. The variations in energy correspond to migrations between slits and edges, and to the gas phase.	28
Figure 13. Graphene-mercaptan interaction energy vs. time step for various representative molecules.	29
Figure 14. Trajectories of a single methyl mercaptan on graphite surface. a) $T = 195$ K and $p = 1.2$ bar, b) $T = 195$ K and $p = 24.8$ bar, c) $T = 298$ K and $p = 3.6$ bar, d) $T = 298$ K and $p = 69.7$ bar.	31
Figure 15. Typical trajectories of single methyl mercaptan in 0.7 nm slit Left: side view, right: top view. a) At $T = 195$ K, $p = 21.5$ bar an adsorption event and limited in-plane diffusion. b) At $T = 298$ K, $p = 167$ bar the adsorption/desorption events and both in-plane diffusion and out-of-plane movement.	33
Figure 16. Radial distribution functions of mercaptans in 0.7 nm slit at a) 195 K, b) 298 K, c) 320 K.....	34
Figure 17. Two-dimensional mean square displacement as a function of simulation time plots for methane and methyl mercaptan at a) 195K, b) 298 K and c) 320 K.	36
Figure 18. Diffusion coefficients vs. pressure at a) 195 K, b) 298 K and c) 320 K.....	37

List of Tables

Table 1. Comparison of features available in analyzed force fields.	15
Table 2. Comparison of number of interaction components considered in United Atom and All Atom representations of methane.	15
Table 3. The OPLS-UA force field non-bonded parameters in UA and AA approaches used in MD simulations.	17
Table 4. Energies of the strongest gas-substrate interactions.	26

1. Introduction

Natural gas (NG) consists mainly of methane, which has hydrogen to carbon ratio higher than any other molecule used as a primary fuel. Of all hydrocarbons NG has the highest energy density per unit mass and the lowest carbon dioxide emission per unit energy, making it an effective and relatively clean alternative for energy applications, especially when considering its lower cost compared to gasoline. Unfortunately, the low density of methane compared to liquid fuels makes its storage more difficult, requiring compression at very high pressures ($p \geq 250 \text{ bar} \approx 3,600 \text{ psig}$, compressed NG, CNG) or liquefaction at very low temperatures ($T \approx -162 \text{ }^\circ\text{C}$, liquefied NG, LNG). Either alternative increases significantly the cost of operation both in terms of production (energy costs, equipment, safety) and storage (bulky tanks and/or cryogenics). In particular, for the case of vehicular use, the use of CNG employs heavy bulky tanks, significantly reducing the available cargo/passenger space.

A promising alternative is to store the fuel as adsorbed NG (ANG). This is possible through physisorption of a gas into a suitable porous solid, designed to hold the fuel at relatively low pressures (e.g., $35 \text{ bar} \approx 500 \text{ psig}$). Highly porous media have sufficient volumetric storage ability to store NG at densities comparable to a high-pressure CNG

tank. The lower operational pressure allows thinner tank walls and a convenient shape [6], resulting in potentially significant cost savings, improvements in safety and reduced cargo volume loss. The difference between storage capacities of adsorbent filled tank and empty tank is shown in Fig. 1.

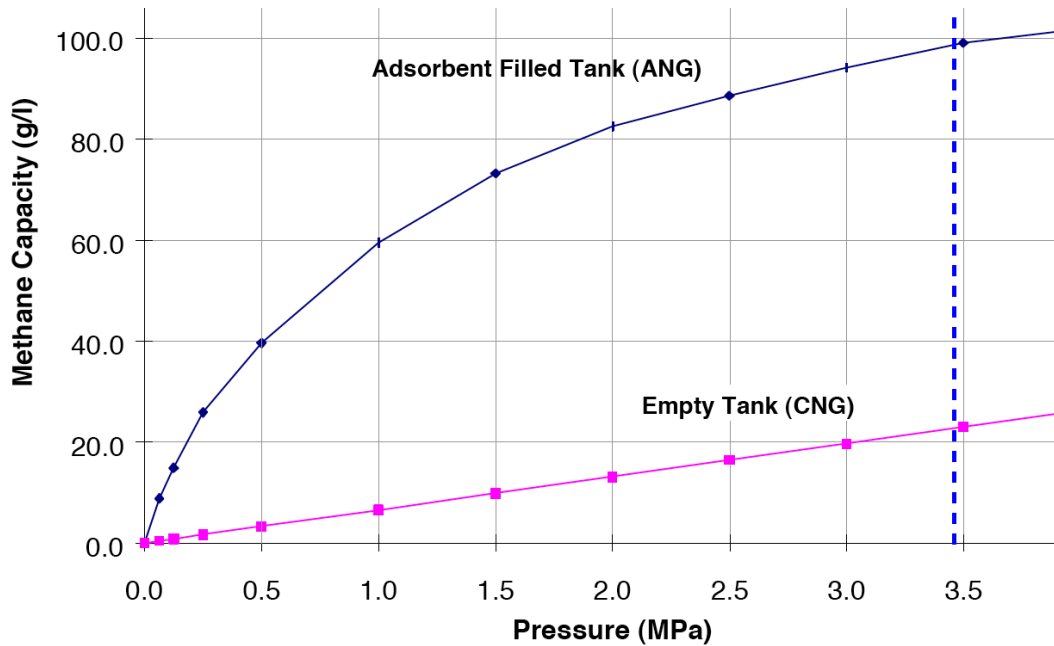


Figure 1. Methane storage capacity per liter of adsorbent as a function of pressure. At pressure equal 3.5 MPa nearly 100 g of natural gas can be stored in a tank filled with adsorbent such as activated carbon. The same amount of condensed natural gas (CNG) can be stored in an empty tank at pressure about 17 MPa.

Carbon-based nano-porous materials appear to be one of the most attractive candidates for room temperature ANG storage for various reasons: (i) low-cost, (ii) no toxicity, (iii) high availability; (iv) low weight; and (v) the fact that isosteric heats of adsorption for methane in activated carbon is 18–20 kJ/mol (2,200–2,400 K) [15],[11], very close to the “Optimum Conditions for Adsorptive Storage” of Bhatia and Myers [5].

Some of the best performing carbons have been manufactured from organic wastes such as corn cob, see Fig.2 [18], and a broad range of experimental methods have been applied to characterize such materials (see [25] and references therein). Furthermore, an understanding of the adsorption mechanism and kinetics at the microscopic level comes from numerical simulations. Monte Carlo [10],[3] and Molecular Dynamics [9] methods have been applied to analyze a wide range of aspects: isotherms of adsorption [23], interaction energies [24],[2], methods of adsorbent structure approximations [20],[7] and migration of gas molecules into and out of the slit volumes [17].



Figure 2. Nanoporous material for vehicular applications—from corn cob to monolith in tank. [18]

Despite all the progress in understanding methane adsorption, very little has been done to understand how other important components of NG act in an ANG setup. Since methane (and other alkanes in NG) is flammable and potentially explosive, significant safety considerations must be satisfied for common use. Methane is odorless therefore it has to be odorized. Typically about 200 ppb of mercaptans are added. Such concentration enables detection of gas in air when the concentration of NG reaches $1/5^{\text{th}}$ of the lower explosive limit (5% by volume in air at 200C, see, e. g., [1]). To the best of our knowledge there are no studies on mercaptans in the context of ANG systems. On the contrary, most current studies of ANG systems are focused on completely removing mercaptans from gas mixtures (e.g., by increasing mercaptan captivation in chemically modified carbons [4]). It would seem inconceivable to us, however, that a significant deployment of ANG could be achieved without the basic safety mechanism of human detection of NG leaks from an ANG system. Therefore, in this work we present a detailed computational effort of the behavior of methane-mercaptan mixtures in nanoporous carbons. Our results indicate that although mercaptans adsorb preferentially as compared to methane, they still are able to migrate with relative ease within sub-nm pores, and that the adsorption is reversible. We estimate that a modest increase in the concentration of mercaptans in NG (prior to adsorption) will be sufficient to permit a desorbed phase to retain the amount of mercaptans above the human detection threshold. Our conclusions further indicate that mercaptans should not pose a major problem contaminating/clogging the adsorbants, thus their use should be possible in ANG systems.

2. Simulation method: Molecular Dynamics

Molecular Dynamics (MD) simulations [21] provide a powerful tool for equilibrium predictions of complex, multiatomic systems. Based on statistical mechanics this computational approach gives the insight to dynamical processes which cannot be calculated analytically and accounts for an important complementary technique to the experimental measurements. The time-dependent evolution of the system, predicted by MD simulations, provides outlook on the continuous motion (set of trajectories) of molecules under investigation. Numerical data gathered during the calculations can be used to derive macroscopic properties which can be compared to the experimental measurements.

In order to run MD simulations there are several steps that have to be followed. First it is required to initialize the system by setting an initial configuration (at time $t = 0$). Initially, the energy of the system is minimized with respect to the molecular coordinates; then the initial velocities are assigned and the dynamic equilibration of the system begins. This means that the forces acting on the atoms are calculated (after every time step) and each of the atoms follows Newton's laws of motion. When the energy of the system fluctuates about constant value throughout the simulations the

trajectories can be analyzed. The details on the main steps of MD simulations are given in sections 2.1-2.4.

2.1. Initialization

In order to start the MD simulations it is necessary to set initial coordinates of particles, which requires basic knowledge on molecular interactions and chemical bonding. When the configuration is build, the program assigns the velocities to each atom so that the total momentum equals zero, and the velocities are then rescaled to satisfy the equipartition theorem, i.e. that the average kinetic energy per degree of freedom follows

$$\langle \frac{1}{2}mv^2 \rangle = \frac{1}{2}k_B T, \quad (1)$$

where v is a component of velocity of a given particle. During simulations of the system consisting of N particles the total kinetic energy undergoes fluctuations, therefore its average defines an instantaneous temperature:

$$T(t) = \sum_{i=1}^N \frac{m_i v_i^2(t)}{k_B N_f}. \quad (2)$$

In order to obtain the desired temperature at time t , the velocities are scaled by factor $[T/T(t)]^{1/2}$.

2.2. Force calculations

For each pair of atoms within a cutoff distance (dependent on the interaction potential between them) the forces are calculated. This is the most time consuming part of the simulations, since for system of N elements there are $N*(N-1)/2$ pair distances. The x -component of the force:

$$f_x(r) = -\frac{du(r)}{dx} = -\left(\frac{x}{r}\right)\left(\frac{du(r)}{dr}\right). \quad (3)$$

If the Lennard-Jones potential is used the expression above becomes:

$$f_x(r) = \frac{48x}{r^2} \left(\frac{1}{r^{12}} - 0.5 \frac{1}{r^6} \right) \quad (4)$$

2.3. Verlet algorithm

The Verlet algorithm is used for the approximation of the positions of particles of simulated system in the next time step. The popularity of the approach is mainly due to its simplicity and the fact that it leads to a little long-term energy drift through the simulations.

A Taylor expansion of the coordinate of a particle around time t :

$$\vec{r}(t + \Delta t) = \vec{r}(t) + \vec{v}(t)\Delta t + \frac{f(t)}{2m}\Delta t^2 + \frac{\Delta t^3}{3!}\ddot{\vec{r}} + O(\Delta t^4), \quad (5)$$

$$\vec{r}(t - \Delta t) = \vec{r}(t) - \vec{v}(t)\Delta t + \frac{f(t)}{2m}\Delta t^2 - \frac{\Delta t^3}{3!}\ddot{\vec{r}} + O(\Delta t^4). \quad (6)$$

Adding up these equation leads to:

$$\vec{r}(t + \Delta t) + \vec{r}(t - \Delta t) = 2\vec{r}(t) + \frac{f(t)}{m}\Delta t^2 + O(\Delta t^4), \quad (7)$$

or

$$\vec{r}(t + \Delta t) \approx 2\vec{r}(t) - \vec{r}(t - \Delta t) + \frac{f(t)}{m}\Delta t^2. \quad (8)$$

The estimation of new positions thus has an error of the order Δt^4 , where Δt is the time step.

At this point it is possible to obtain the velocities:

$$\vec{r}(t + \Delta t) - \vec{r}(t - \Delta t) = 2\vec{v}(t) + O(\Delta t^3), \quad (9)$$

or

$$\vec{v}(t) = \frac{\vec{r}(t + \Delta t) + \vec{r}(t - \Delta t)}{2\Delta t} + O(\Delta t^2). \quad (10)$$

Moving the algorithm forward into the next time step, the current positions become old ones and the new positions become current.

2.5. Periodic boundary conditions

In general, one is limited to simulation boxes of relatively small size. Unless surface effects are of particular interest, periodic boundary conditions (PBC), in which there are no edges, are used to better approximate the conditions in large systems. The total energy of the computed system with PCB is calculated according to the equation (11)

$$U_{tot} = \frac{1}{2} \sum_{i,j,n}^{N_M} (|\vec{r}_{ij} + \vec{n}L|), \quad (11)$$

where N_M is the number of molecules at any periodic box, L is the lateral dimension of the periodic box and \vec{n} stands for an arbitrary vector of 3 integer numbers, among which the prime over the sum indicates that the term with $i = j$ is to be excluded when $\vec{n} = 0$.

Of course, it is important to bear in mind the imposed artificial periodicity when considering properties which are influenced by long-range correlations. Special attention must be paid to the case where the potential range is not short: for example for charged and dipolar systems.

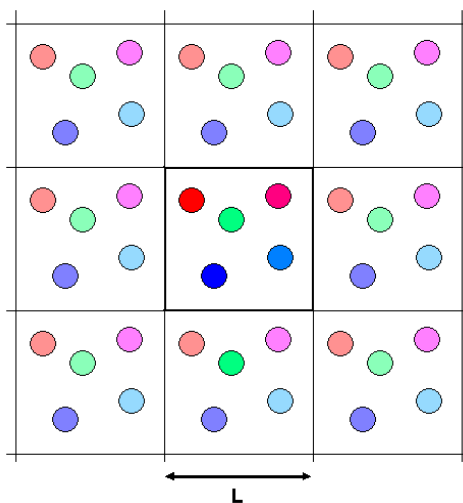


Figure 3. Two-dimensional periodic domain showing unit cell (in the center of the scheme) and its images (surrounding replicas).

In a system of molecules adsorbed on the planar surface, the PBC in two dimensions, x and y , are applied (Fig. 3), while the third, z , direction is open, i.e. having no boundary conditions. This convention is known as slab boundary conditions.

3. Simulation setup

As a model for activated carbon we considered graphene-based slit pores and performed Molecular Dynamics (MD) simulations in the canonical ensemble (*NVT*). A parallel MD code, NAMD, [19] was applied, with time step equal 1 fs. A simulation box of 14.0 nm x 10.0 nm x $3H$, where H is the pore width, contained the adsorbent and gas molecules as depicted in Fig. 4. Periodic boundary conditions were used in all directions. The simulation box contained three parallel layers of graphene of dimensions 10.0 x 10.0 nm², each pair of sheets separated by $H = 0.7$ nm (graphene center to center distance). Such configuration of the box was deliberately chosen for three reasons. First, it allows observing and quantifying the adsorption at the pore edges which is totally missed in the simulation with infinite pore walls. Second, the free box space (outside the pore) allows the molecules' migration between different pores, a process which again cannot be observed if the pore wall surface is infinite. Lastly, a pore width of 0.7 nm maximizes the adsorption potential depth, thus making it the most critical in terms of studies of adsorption reversibility. The systems were allowed to stabilize for 5 ns before the production runs began (checked for equilibration by verifying energy stability in a function of time). The properties of the system were obtained from the last 0.5 ns of the

simulations. Since MD operates in the canonical ensemble the pressure of the gas must be determined *a posteriori* for each run after equilibration is achieved.

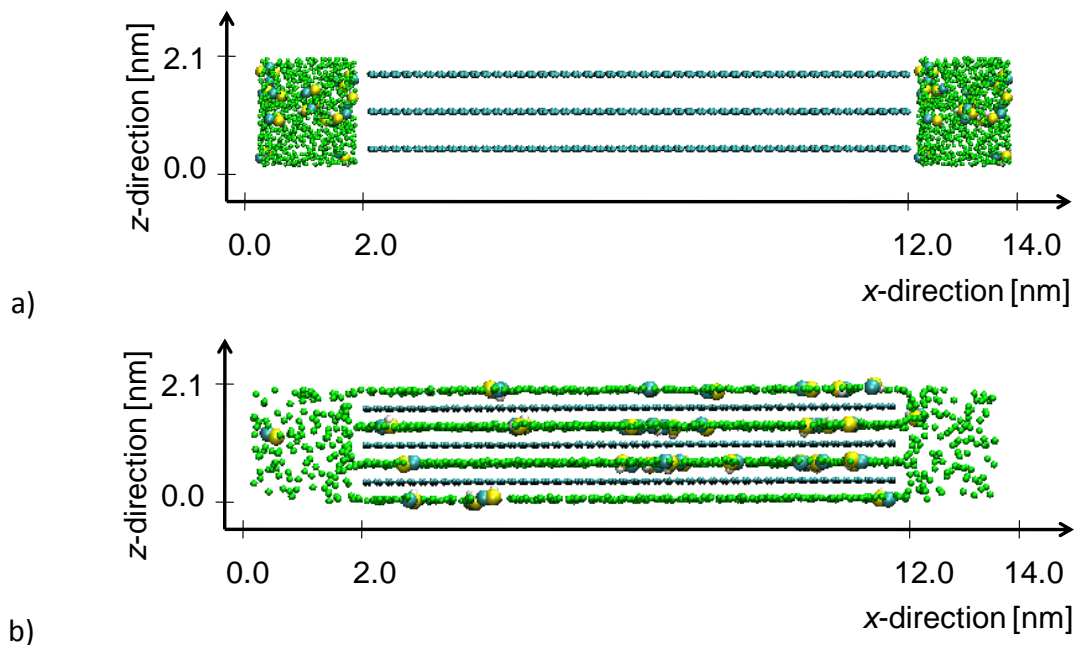


Figure 4. Side view of the $14.0 \times 10.0 \times 21.0 \text{ nm}^3$ simulation box containing three graphene sheets (blue circles), methane (small green circles) and methyl mercaptan (larger, blue and yellow circles). The graphene sheets are $10.0 \times 10.0 \text{ nm}^2$, leaving space for a gas phase in equilibrium with the adsorbed phase. a) the initial placement of gas molecules beyond slit volume. b) Stabilized system. Periodic boundary conditions were used in all directions.

The simulations procedure is as follows: The initial configuration (Fig. 4. a.) consisted of a random placement of methane and mercaptan molecules in the volume outside the slits. Depending on pressure and temperature, the analyzed systems contained 1,836 to 2,550 ($T = 195 \text{ K}$, dry ice temperature), 1,326 to 2,040 ($T = 298 \text{ K}$, room temperature), and 1,224 to 1,938 ($T = 320 \text{ K}$) gas molecules in a constant proportion (98% methane, 2% methyl mercaptan). At energetic and conformational equilibrium (Fig. 4.b.) gas

molecules adsorbed within slits and on the pores edges and some remained in gas phase in the volume outside the slits. This is shown schematically in Fig. 5 (projection along the y direction). The amount of adsorbed molecules was calculated from the coordinates of molecules for each frame in the simulations. The adsorption isotherms were calculated and averaged over the frames of the production runs. The analysis of methane and mercaptan trajectories and gas-slit interaction energies were also obtained from the last 0.5 ns of simulations. Pressures were obtained from the density of molecules in the gas phase (i.e., $x < 1$ nm and $x > 13$ nm in Fig. 5) using the ideal gas law.

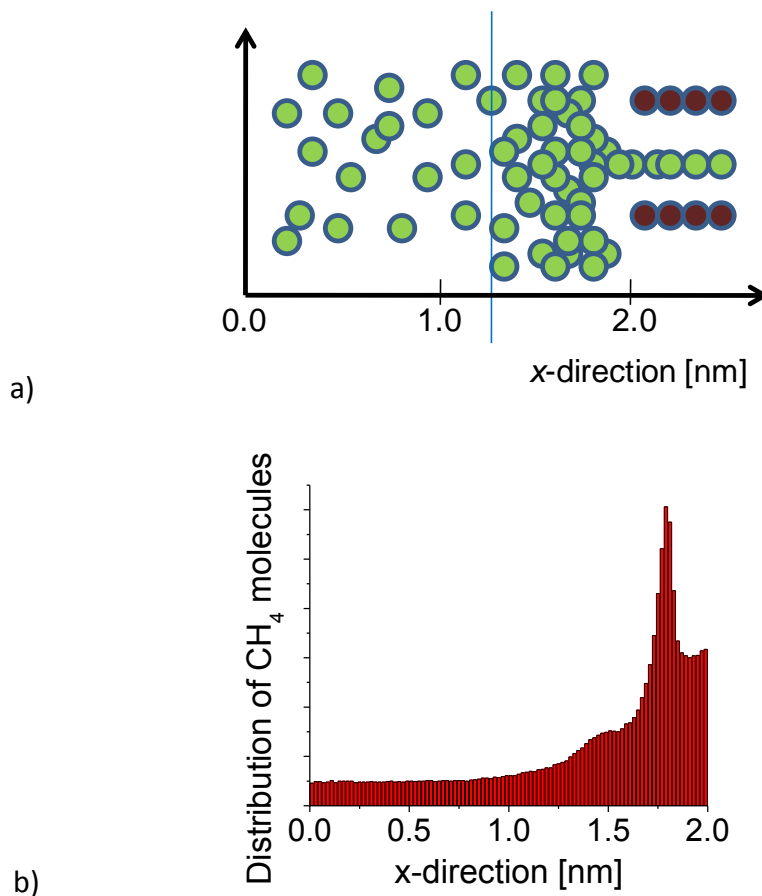


Figure 5. a) Gas distribution on the edge of a typical slit. b) Corresponding density profile of molecules in x-direction (outside the slit, $x < 2$ nm).

4. Choice of force field

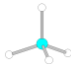

Several force fields (sets of interaction parameters) are available in literature. For simulations presented in this chapter, the initial search through available documentation focused on three most standard force fields: OPLS (Optimized Potentials for Liquid Simulations) [12], CHARMM (Chemistry at HARvard Molecular Mechanics)[13], and TraPPE (Transferable Potentials for Phase Equilibria)[14]. CHARMM was originally parameterized to describe large biological systems such as proteins and lipids. The description of small molecules, including mercaptans, is not precise and some of the angular parameters are missing. Additionally, this force field does not provide data for United Atom approach. TraPPE gives the United Atom parameters for most organic compounds, but the All Atom description of heteroatomic systems has not been developed. The OPLS force field contains all interaction parameters for both methane and methyl mercaptan, in both AA and UA approaches; therefore it was chosen to describe the interactions in our simulations. The schematic comparison of the availability of interaction parameters for simulations of methane-methyl mercaptan mixture in carbon nanopores is presented in Table 1.

Table 1. Comparison of features available in analyzed force fields.

	All Atom	United Atom	Remarks
OPLS	+	+	
CHARMM	+	-	No angular parameters for short mercaptans
TraPPE	+/-	+	AA parameters for mercaptans not available

The United Atom (UA) approach was used. The interaction components for simulations of methane molecule accounted for in AA and UA approaches is presented in Tab. 2. A significant reduction of interactions (and corresponding parameters) in UA simulations leads to a 5-fold reduction of the simulation time with respect to time- and resource-consuming All Atom (AA) simulations.

Table 2. Comparison of number of interaction components considered in United Atom and All Atom representations of methane.

Methane	All Atom 	United Atom 
# of sites	5	1
# of bonds	4	0
# of angles	6	0
# of dihedrals	0	0

In OPLS-UA representation methane molecule is described as a single super-atom. Methyl mercaptan consists of three units: a -CH₃ superatom, sulfur atom and explicit hydrogen atom in the thiol group (see Fig. 6). Non-bonded solid-fluid and fluid-fluid interactions were modeled by a Lennard-Jones (12-6) potential and calculated with a 1.5

nm cutoff. Partial charges of individual atoms/superatoms were included, but polarization was not taken into account.

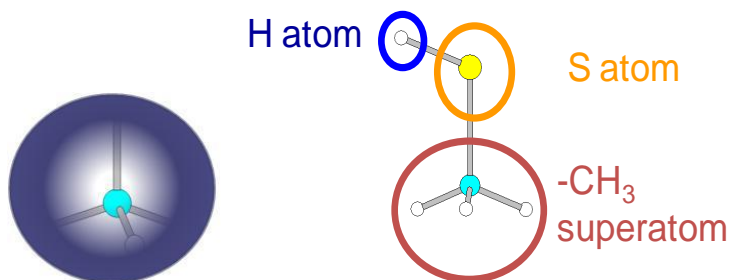


Figure 6. OPLS-UA representation of methane (left) and methyl mercaptan (right).

It should be noted, that NAMD package uses the analytical form of potential functions which is directly compatible with CHARMM and AMBER force field notation, but not with the OPLS formalism (Eq.12). Therefore, the OPLS parameters had to be rescaled to match the equations implemented in NAMD code (Eq. 13)

$$U(r_{i,j}^{a,b}) = 4\varepsilon^{a,b} \left[\left(\frac{\sigma_{i,j}^{a,b}}{r_{i,j}^{a,b}} \right)^{12} - \left(\frac{\sigma_{i,j}^{a,b}}{r_{i,j}^{a,b}} \right)^6 \right], \quad (12)$$

$$U(r_{i,j}^{a,b}) = \varepsilon^{a,b} \left[\left(\frac{d_{i,j}^{a,b}}{r_{i,j}^{a,b}} \right)^{12} - 2 \left(\frac{d_{i,j}^{a,b}}{r_{i,j}^{a,b}} \right)^6 \right], \quad (13)$$

where $d_{ij} = \sigma_{ij}(2)^{1/6}$. The set of non-bonded parameters used in MD simulations is given in Table 3.

Table 3. The OPLS-UA force field non-bonded parameters in UA and AA approaches used in MD simulations.

United Atom	σ [nm]	ϵ/k [K]	q [e]
CH ₄ superatom	0.373	148.045	0.000
S (-SH)	0.335	125.889	-0.450
H (-SH)	0.000	0.000	0.270
-CH ₃ superatom	0.378	104.236	0.180
C (graphene)	0.340	28.000	0.000

All Atom	σ [nm]	ϵ/k [K]	q [e]
C (CH ₄)	0.312	33.235	-0.240
H (CH ₄)	0.220	5.107	0.060
S (-SH)	0.355	125.889	-0.335
H (-SH)	0.000	0.000	0.155
C (-CH ₃)	0.350	33.235	0.000
H (-CH ₃)	0.250	15.107	0.060
C (graphene)	0.340	28.000	0.000

Figure 7.a shows specific ways of placing methane molecules over graphitic surface. The two most distinct configurations of All Atom methane over the graphitic surface are: 1) “tripod down” orientation (three hydrogen atoms are located closest to the surface), and 2) “tripod up” (the carbon-hydrogen bond is directed perpendicular to the substrate and three remaining hydrogen atoms placed furthest from the surface). In case of United Atom representation the 5-atom molecule is considered as a spherical superatom, therefore it is impossible to distinguish real molecule orientation; therefore

its location over the graphite surface is characterized by only one parameter, the distance between molecule's center of mass and the surface.

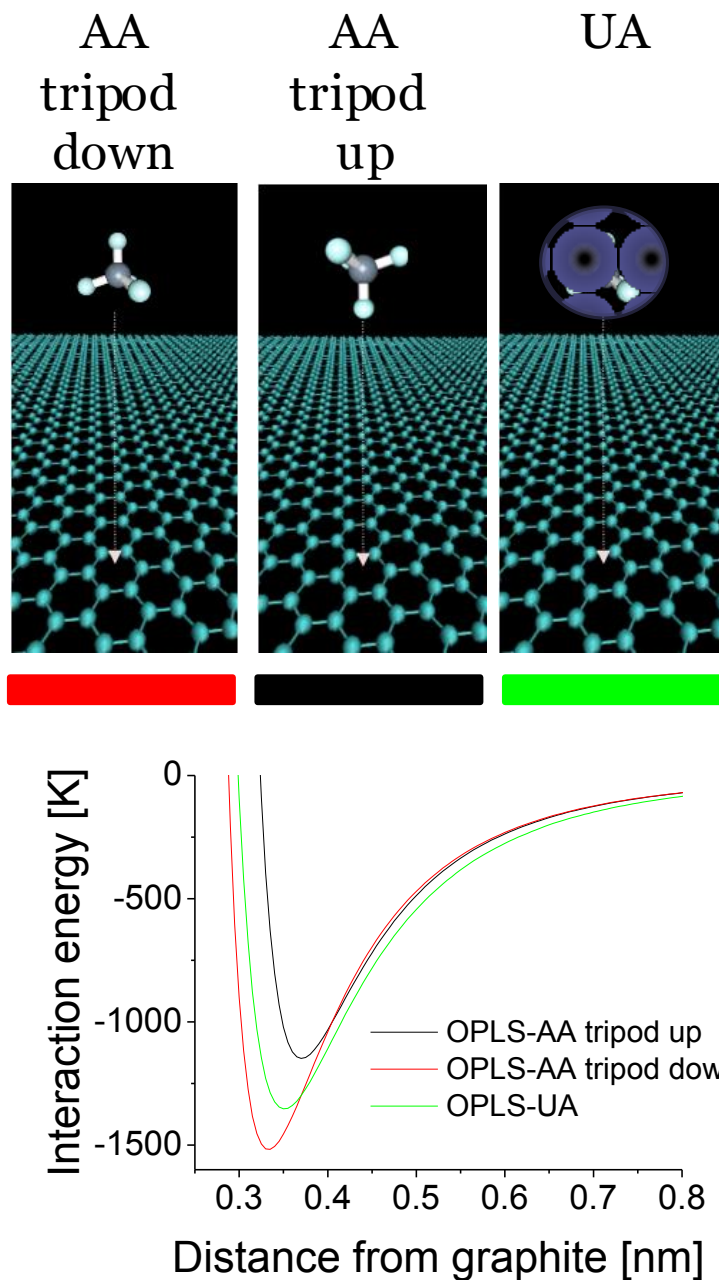


Figure 7. a) All Atom representation of methane: tripod down, tripod up and United Atom molecule, b) Comparison of the interaction energies between three representations.

Figure 7.b compares the methane-graphite interaction energies as a function of distance of methane center of mass (central carbon atom in AA representation) from graphite, in three configurations specified above. The Lennard-Jones 12-6 form of potential with OPLS parameters was used, with a cutoff equal 1.5 nm. As it could be expected, the strongest interaction with substrate is observed for the “tripod down” configuration while in the case of the “tripod up” orientation the depth of the potential well is the smallest. The energy minimum for UA model is placed in between the two extreme AA situations.

Figure 8 compares the methane-graphite interaction energies calculated using OPLS parameters with data available in the literature [3],[8],[2],[16]. Two configurations are analyzed: “tripod down” (AA approach, Fig.8.a) and UA approximation (Fig.8.b). In both cases the OPLS non-bonded parameters were implemented into Lennard-Jones 12-6 potential while the referenced solid-fluid parameters were inserted into the Steele 10-4-4 potential. No significant difference between the literature data and our calculations has been found. Strong overlapping of the plots is visible. This confirms that the OPLS-AA and OPLS-UA parameters are consistent with force field parameters previously used in numerical studies of methane adsorption and auto-organisation on graphite.

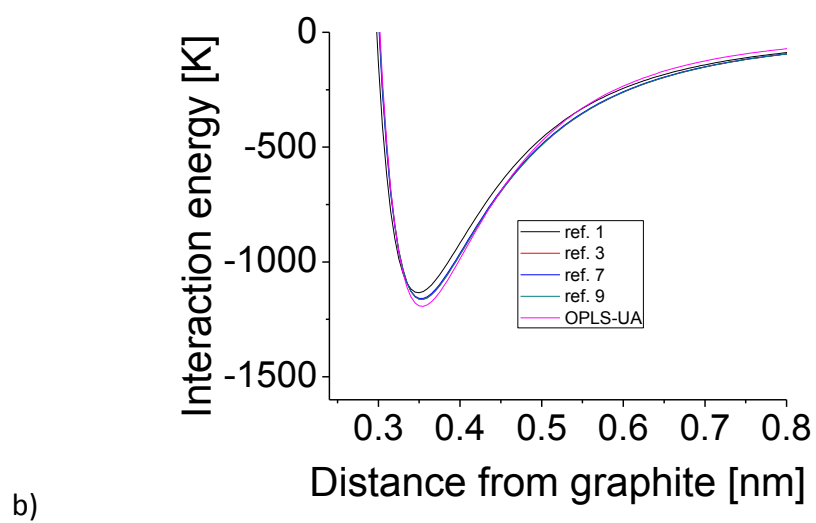
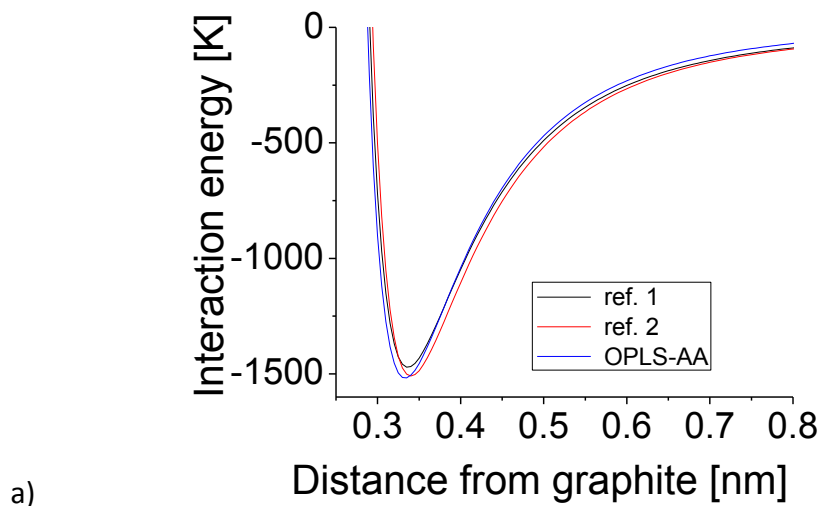
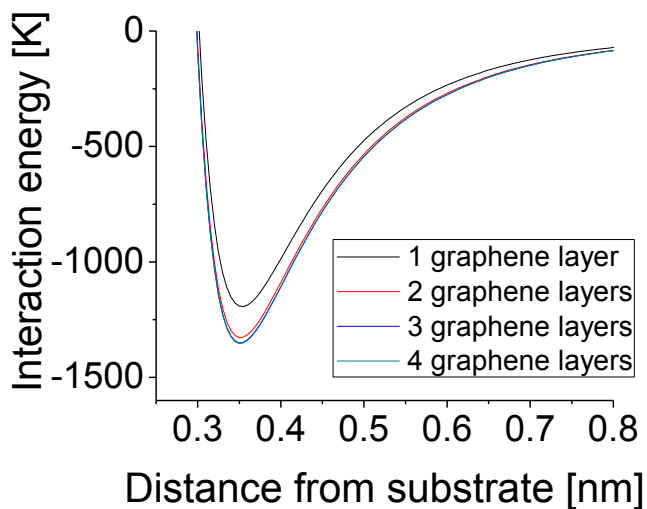
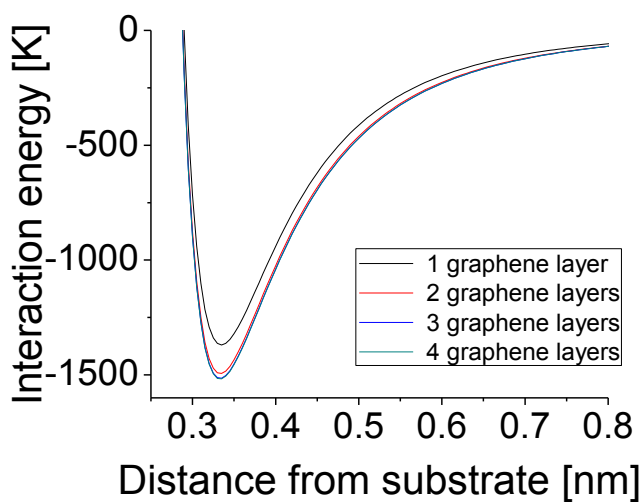


Figure 8. Comparison of methane–graphite interaction energy calculated using OPLS parameters with selected data available in literature: a) AA approach, b) UA approach.

We have also verified if the increase of the strength of methane-surface interaction with increasing number of graphene layers forming the substrate is correctly reproduced when OPLS parameters are used. Figure 9 shows the variation of methane-substrate interaction in both UA and AA models when successive graphene layers are added. There is no significant change in gas-substrate interaction energy when the substrate contains a stack of three or more graphene sheets. This result is consistent with the literature data showing that to simulate interactions of molecules with infinite (in depth) graphite surface it is sufficient to model the graphite using only four layers of graphene, at least if the cutoff of interactions is equal 1.5 nm.



a)



b)

Figure 9. Energy of methane interaction with 1, 2, 3, and 4 layers of graphene: a) UA representation of methane, b) AA representation of methane (tripod down configuration).

The simulations were carried out at 195 K (below the boiling point of methyl mercaptan, 279 K), at 298 K and 320 K. In order to verify the choice of force field parameters for methyl mercaptan, test simulations of gas mixtures without graphene were first conducted. Two molar fractions of thiols were chosen: 0.065 and 0.019 and systems were equilibrated at the three chosen temperatures. At room temperature and 320 K

the mixtures of gases are homogeneous at both thiol concentrations. At 195 K and high methyl mercaptan content the odorant molecules aggregate (Fig. 10.a), but is absent at the lower thiol concentration ($\sim 2\%$, Fig. 10.b). These results are reasonable and give additional credence to the parameters and methods employed.

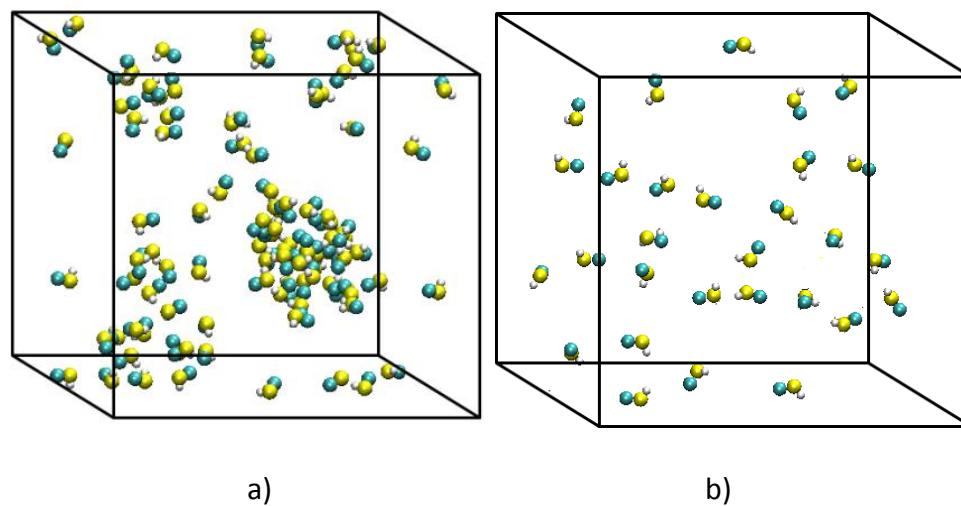
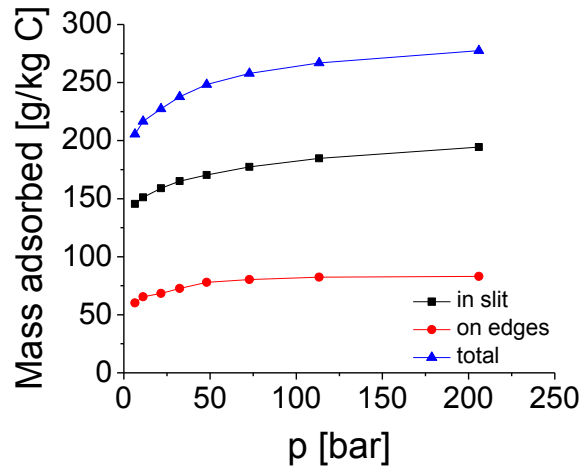


Figure 10. Snapshots of methyl mercaptan-methane mixture at 195 K (below its boiling point) and molar fractions of CH₃SH equal a) 0.065, b) 0.019. Aggregation of mercaptans at the higher concentration is seen. For clarity only CH₃SH molecules are shown.

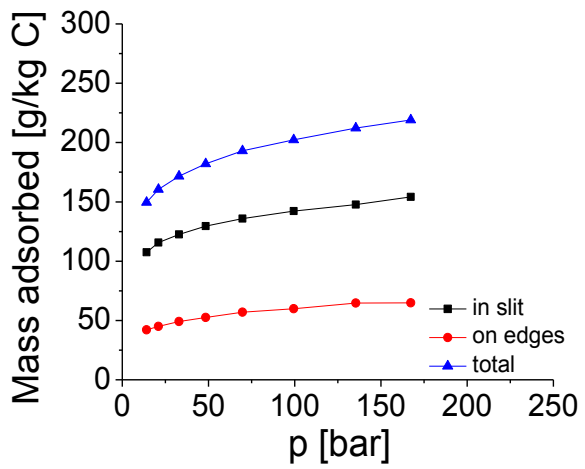
5. Results and discussion

5.1. Adsorption isotherms

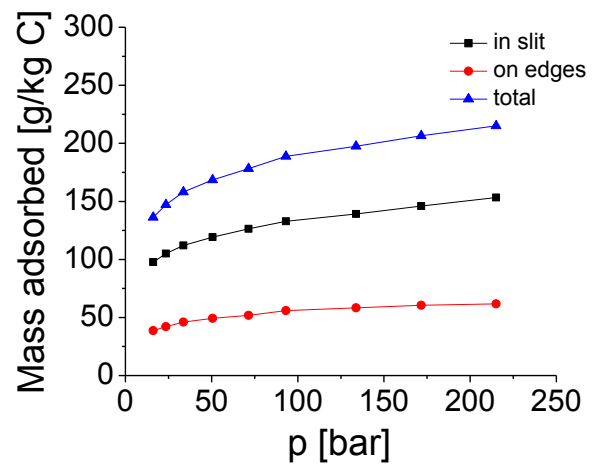
Figure 11 shows the adsorption isotherms of mixtures of methane (98 %) and methyl mercaptan (2 %) in slit-shaped graphitic pores separated by 0.7 nm, at 195 K, 298 K and 320 K. In all cases we observe significant adsorption not only in the space between the graphene sheets (inside the slit-shaped pores, black curves), but also on the edges of the pores (red curves). The significance of edge-adsorption is evident, giving about 1/3 of the total mass adsorbed (blue curves) for the geometry under consideration.



a)



b)



c)

Figure 11. Adsorption isotherms of methane-mercaptan mixtures in 0.7 nm slits at a) 195 K, b) 298 K, c) 320K.

5.2. Adsorption energy: maximum value and fluctuations, mobility

In this section we present the analysis of plots of solid-fluid interaction energies as functions of simulation frame number (1 frame = 100 fs) for methane- and methyl mercaptan-graphene pairs separately at 195 K, 298 K and 320 K and various pressures. For each system considered the strongest interaction energy is observed when gas molecule is present between two graphitic sheets. The values of the strongest interaction energies between methane-substrate and methyl mercaptan-substrate pairs (averaged over the number of molecules) are presented in Table 4. Fluctuations of the interaction energies are coupled with capability of both methane and mercaptan to migrate between the gas phase and inner volume of the slit (Figs. 12 and 13).

Table 4. Energies of the strongest gas-substrate interactions.

196 K	Methane	Thiol	298 K	Methane	Thiol	320 K	Methane	Thiol
Pressure [bar]	Energy [K]	Energy [K]	Pressure [bar]	Energy [K]	Energy [K]	Pressure [bar]	Energy [K]	Energy [K]
6.5	-2,367	-4,056	21.0	-2,299	-4,101	16.2	-2,422	-4,147
21.5	-2,264	-4,052	48.8	-2,300	-4,096	33.7	-2,422	-4,147
48.1	-2,178	-3,993	99.5	-2,155	-4,071	71.5	-2,421	-4,147
113.0	-1,956	-3,939	167.0	-1,917	-3,982	215.0	-2,419	-4,146

Methyl mercaptan's size (< 0.437 nm) could allow relatively free molecular movement in a 0.7 nm pore. However the thiol group interacts more strongly with the graphene (nearly 2 times stronger compared to methane-graphene), which could hinder its motion and make the mercaptan adsorption irreversible. Given the small number of mercaptans (and, in consequence, poor statistics for that component of the mixture), it is difficult to obtain reliable adsorption/desorption isotherms for this component. We thus focused on performing an energetic and dynamical analysis of the gas mixture.

Figures 12 and 13 show the time evolution of the interaction energy between representative methane (Fig. 12) and methyl mercaptan (Fig. 13) molecules and graphene slits at lowest and highest pressures achieved at each simulation temperature, e.g., 6.5 bar and 206 bar at 195 K, 14.1 bar and 167 bar at 298 K, 16.2 bar and 215 bar at 320 K. In all cases methane molecules reveal dynamical behavior, and mobility increases as the gas pressure increases due to saturation of the deepest adsorption sites.

The methyl mercaptan-substrate interaction energies also fluctuate significantly throughout simulation time, even at temperature as low as 195 K (Fig. 13). Despite high substrate-adsorbate interaction energy, mercaptan molecules remain mobile and change their positions with respect to the slit. More significant energy fluctuations appear at room and higher temperature. The mercaptan-graphene interaction energy for some representative molecules was correlated with the changes in the center of mass positions for the odorants in the z direction.

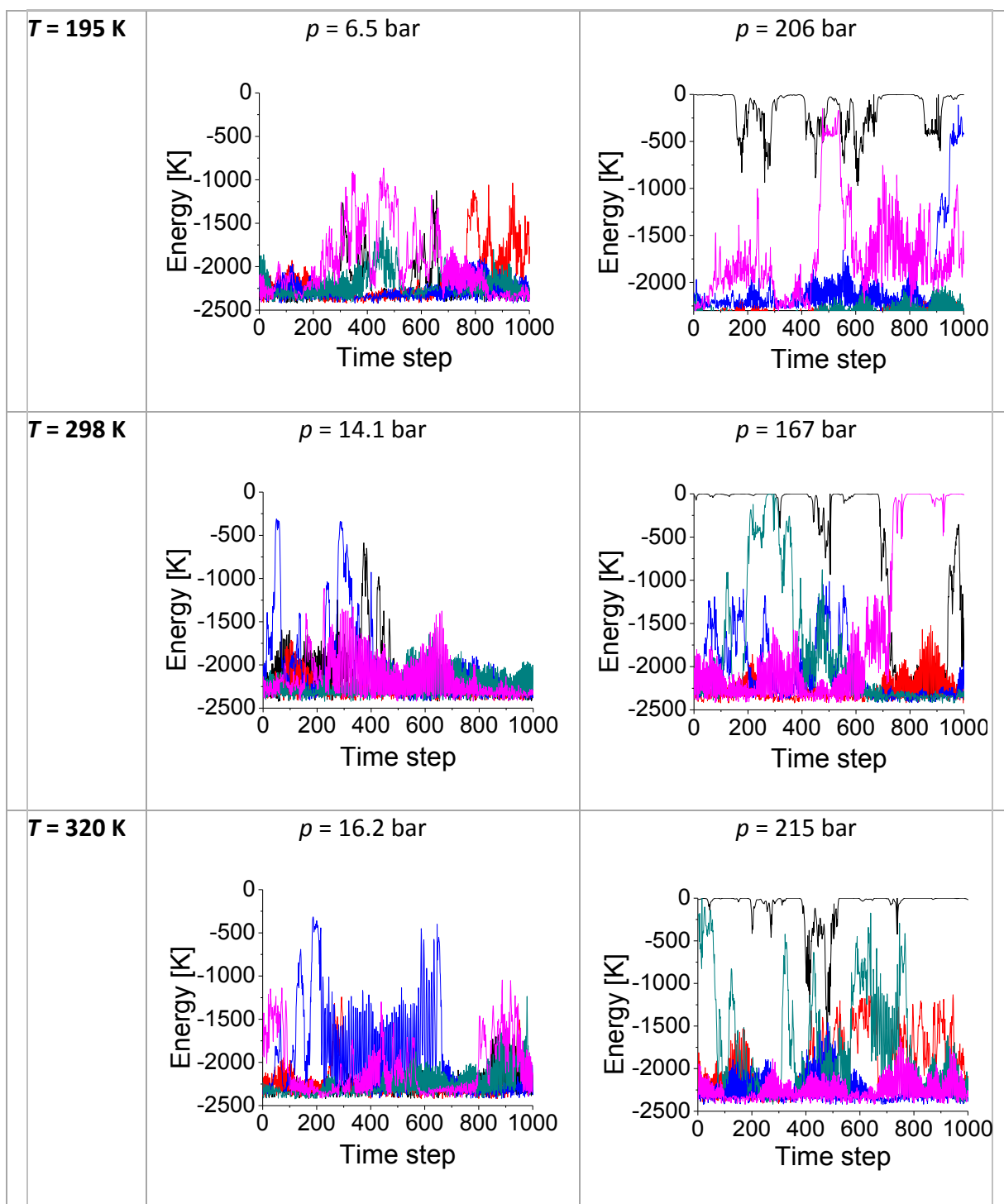


Figure 12. Graphene-methane interaction energy vs. time step for various representative molecules. The variations in energy correspond to migrations between slits and edges, and to the gas phase.

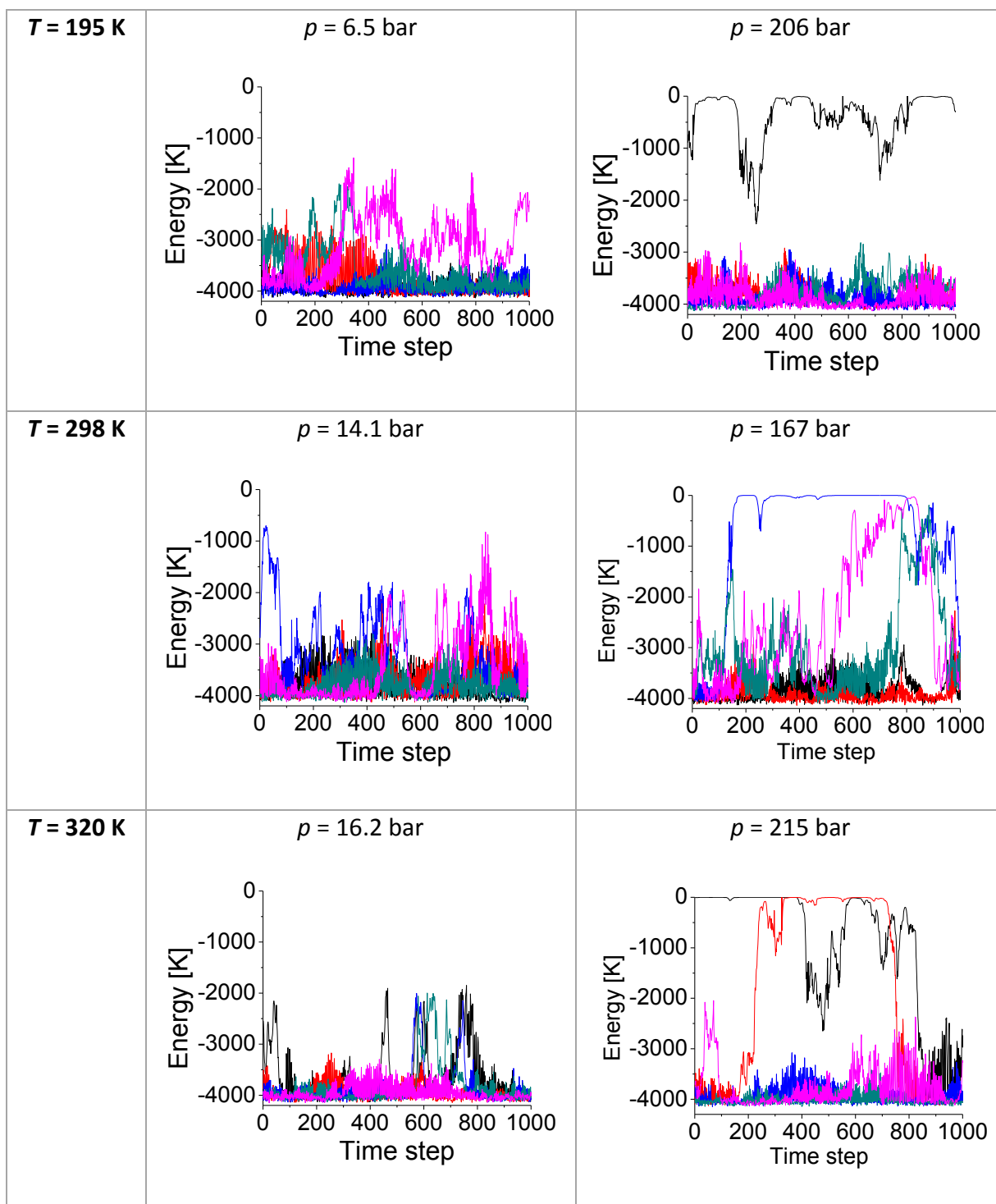


Figure 13. Graphene-mercaptan interaction energy vs. time step for various representative molecules.

5.3. Diffusion in adsorbed methane-methyl mercaptan mixtures

5.3.1. Graphene surface

We first analyzed trajectories of molecules in a reference system, consisting of a single graphene plane. In this case the simulation cell, similar to that depicted in Fig. 4, consisted of two graphene plates separated by 10.0 nm, therefore considered as isolated surfaces. Figure 14 shows typical trajectories of mercaptan adsorbed in such system. At low temperatures and low pressures mercaptan molecules tend to freely migrate over the surface of the adsorbent. The migration is significantly reduced at higher pressures due to the saturation of substrate with methane molecules yielding hindered motion of the mercaptans. At room temperature we observe significant in-plane motion even at surface saturation. Furthermore we observe significant number of adsorption/desorption events, and some mercaptans in the gas phase at higher pressures.

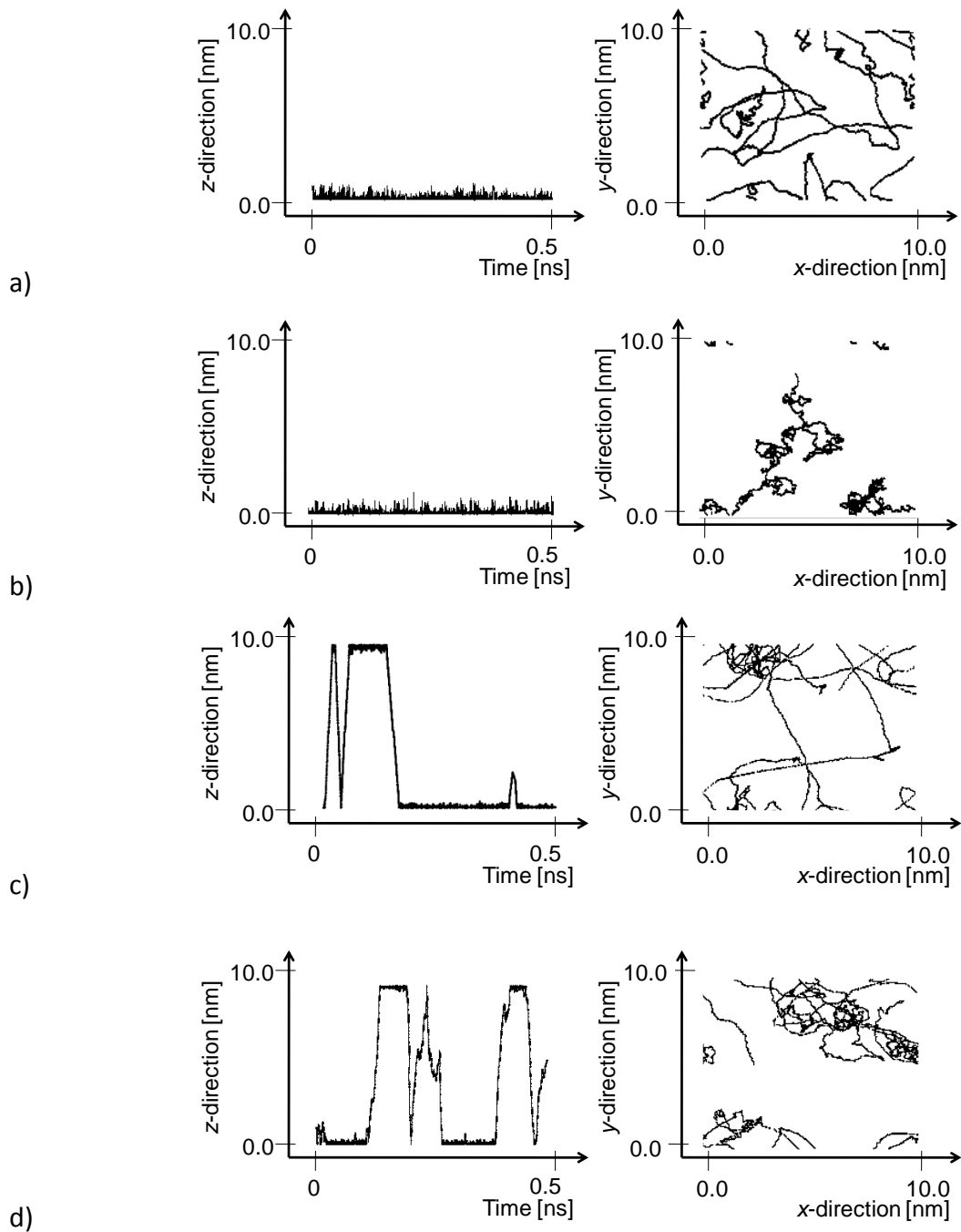


Figure 14. Trajectories of a single methyl mercaptan on graphite surface. a) $T = 195$ K and $p = 1.2$ bar, b) $T = 195$ K and $p = 24.8$ bar, c) $T = 298$ K and $p = 3.6$ bar, d) $T = 298$ K and $p = 69.7$ bar.

5.3.2. 0.7 nm slit-shaped pores

We now consider the mobility of methane and methyl mercaptan molecules adsorbed in narrow, 0.7 nm wide pores. As mentioned earlier, such geometry provides the most severe conditions (geometric and energetic) for adsorption and generates an extreme adsorption scenario: highest adsorbed phase density and highest probability for mercaptans to be trapped inside the pores. Figure 15 shows the trajectories of mercaptan molecules in the simulation box, at moderate pressures and two temperatures: 195 K and 298 K. At 195 K mercaptan molecules initially diffuse into the pores but then their motion remains constrained to a limited fraction of the pore volume. At 298 K mercaptan mobility is significantly higher; molecules rapidly move inside the slit and are able to probe a wide area between the slits walls. In consequence they can also desorb from one pore into the gas phase and then adsorb into another one (Fig. 15, lower left panel), i.e., three-dimensional movement is possible.

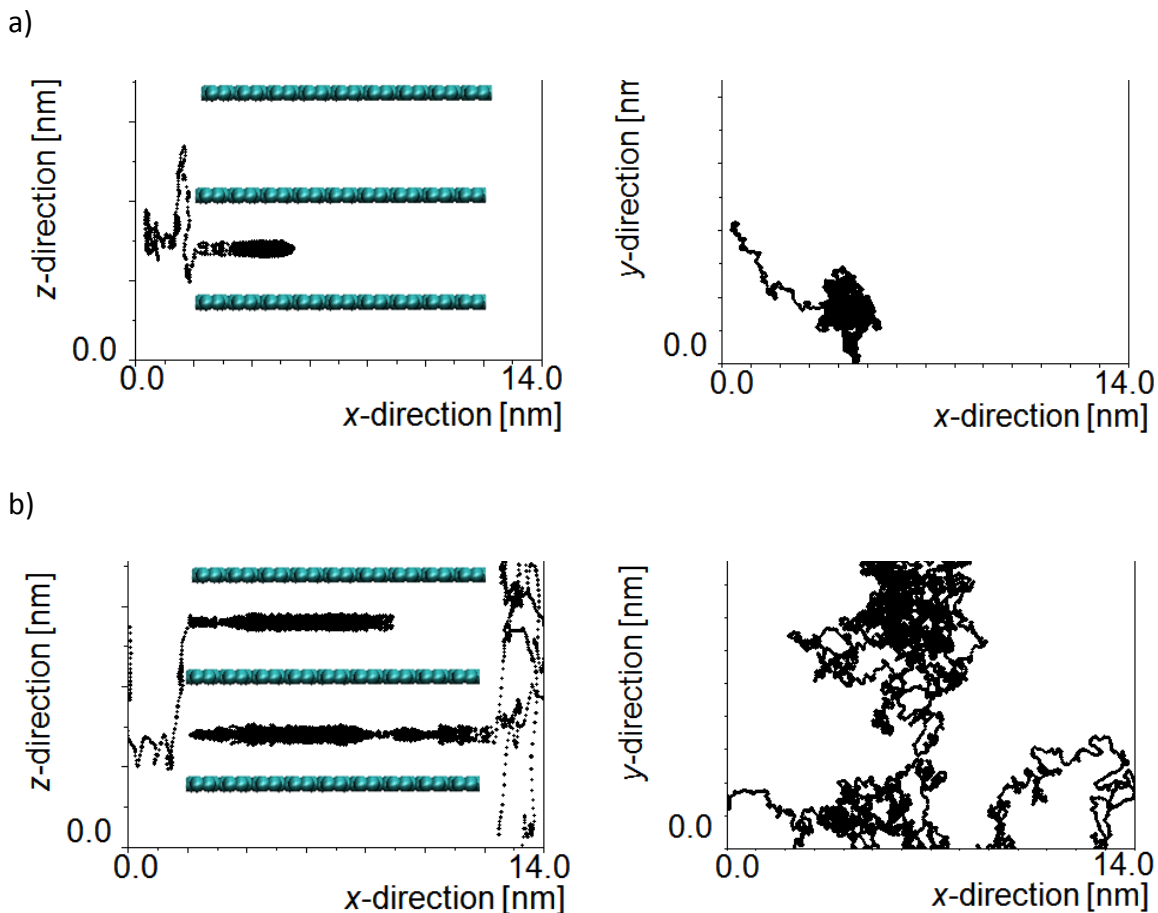
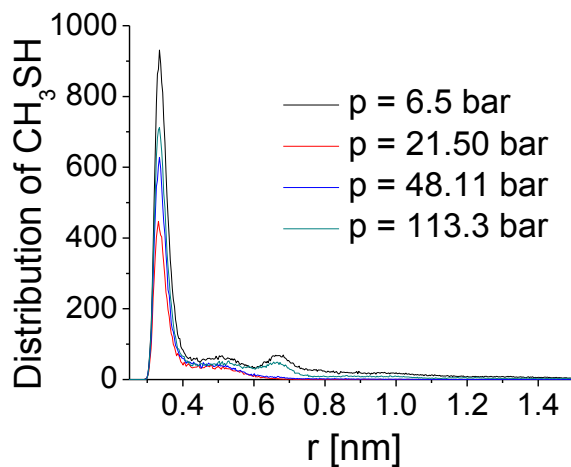
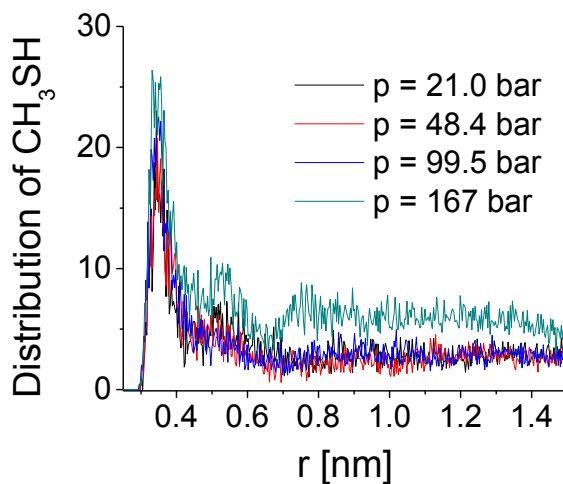


Figure 15. Typical trajectories of single methyl mercaptan in 0.7 nm slit Left: side view, right: top view. a) At $T = 195$ K, $p = 21.5$ bar an adsorption event and limited in-plane diffusion. b) At $T = 298$ K, $p = 167$ bar the adsorption/desorption events and both in-plane diffusion and out-of-plane movement.

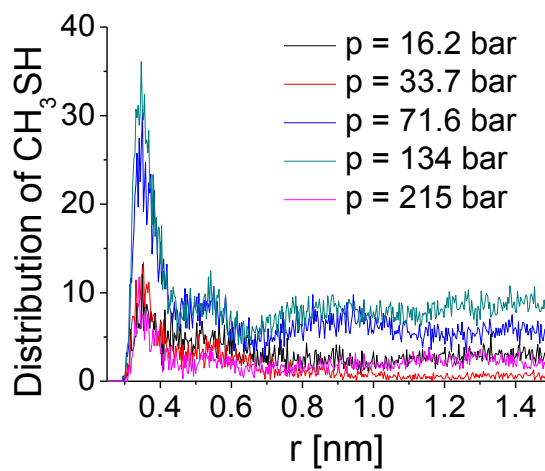
Figure 16 shows the radial distribution functions for mercaptan molecules in a 0.7 nm slit pore at 195 K, 298 K and 320 K at various pressures. At 195 K the peaks of the distribution function show tendency of the mercaptans to aggregate, contrary to what happens in the 2 % methane-mercaptan mixtures in absence of the adsorbant (i.e., in gas phase). At higher temperatures, the relatively less structured distribution function is indicative of absence of aggregation.



a)



b)



c)

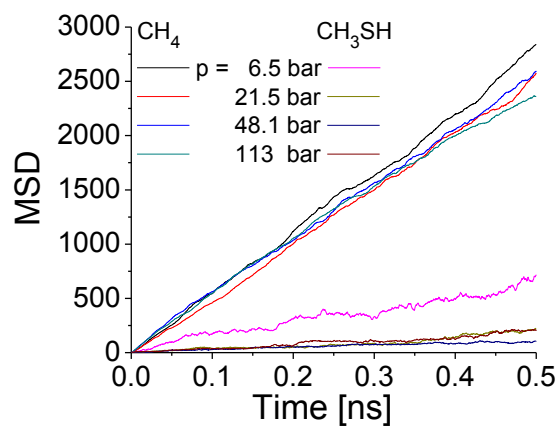
Figure 16. Radial distribution functions of mercaptans in 0.7 nm slit at a) 195 K, b) 298 K, c) 320 K.

The dynamical behavior of methane and methyl mercaptan inside the graphitic slits was further analyzed via the determination of the molecules' mean square displacement (MSD). We considered both MSDs in two dimensions (2D, the in-plane motion within a slit), and three dimensions (3D, including migration between pores). In all cases analyzed, MSDs grow linearly in time within the margin of error, indicating a normal diffusion regime. Figure 17 shows in detail the 2D MSD's for both methane and mercaptans at various temperature and pressure values. Methane's migration inside of the slit volume decreases with increasing pressure. At 195 K mercaptan migration inside the slit is the strongest at lowest gas pressure. With increasing temperature the mobility of mercaptans depends on the amount of gas adsorbed. However, the differences become smaller at and above the critical temperature. Finally, at 320 K no correlation is seen between mercaptans' mobility and the system pressure change.

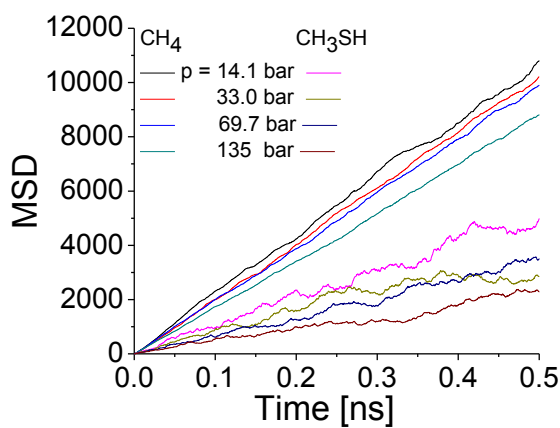
Given the linear MSD vs. t observed in all cases, we calculated 2D and 3D self-diffusion coefficients of methane and methyl mercaptan, according to the relation:

$$D = \lim_{t \rightarrow \infty} \frac{1}{2dt} (MSD), \quad (14)$$

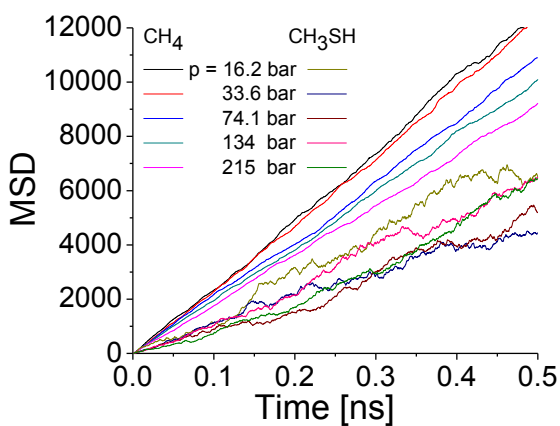
where d is the dimensionality of the problem (2 or 3) and t is the timestep. The resulting diffusion constants are shown in Fig. 18.



a)



b)



c)

Figure 17. Two-dimensional mean square displacement as a function of simulation time plots for methane and methyl mercaptan at a) 195K, b) 298 K and c) 320 K.

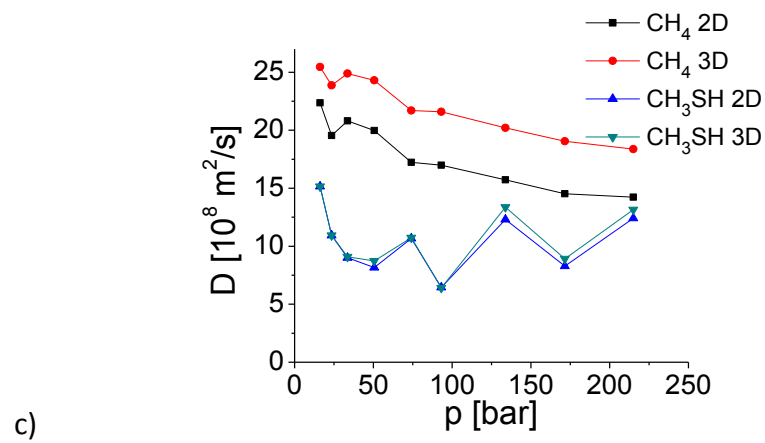
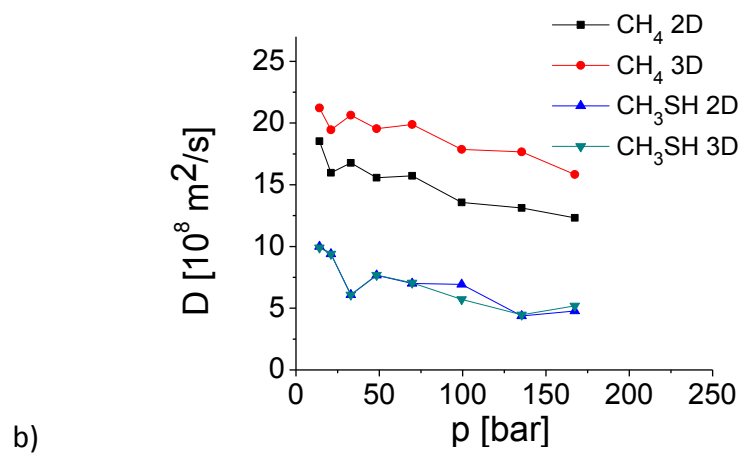
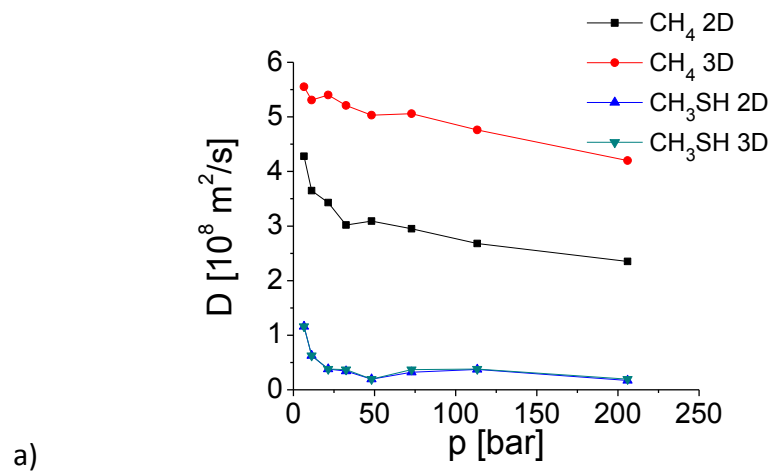


Figure 18. Diffusion coefficients vs. pressure at a) 195 K, b) 298 K and c) 320 K.

5.4. Required enhancement of mercaptan concentration in natural gas

In order to detect natural gas leaks, the concentration of mercaptans in the gas phase should be above ca. 200 ppb (see discussion in Section 1). Since mercaptans bind to graphite more strongly than methane (Table 4), it is necessary to increase their concentration in the adsorbed phase so that any amount desorbed contains at least the required concentration. Here we present a *qualitative* assessment of mercaptan concentrations for detectability; therefore, because of important safety considerations, experiments will inevitably have to yield *quantitative* detectability results. To evaluate the required mercaptan concentration we have assumed that:

- (i) Interaction between adsorbed molecules will be neglected (a decent, though not *quantitatively* correct, assumption for supercritical adsorption);
- (ii) Quantum mechanical effects are small (a very reasonable assumption for relatively heavy molecules at the temperatures considered. The thermal wavelength for methane at room temperature $\Lambda = \sqrt{h^2/2\pi mk_B T} \approx 0.02 \text{ nm}$, much smaller than any other distance considered in the present study);
- (iv) The molar volume of the adsorbed phase is much smaller than that of the gas phase (reasonable except at pressures near saturation); and
- (v) The ideal gas law applies for the gas phase.

With the simplifying assumptions (i)–(v) above, integration of the Clausius-Clayperon equation [26] yields, for each species:

$$\ln P = -\frac{\Delta H^{ads}}{RT} + C \quad (15)$$

where P is the partial gas pressure, ΔH^{ads} is its isosteric heat of adsorption, and C is a species-depends constant. The ratio of concentration in the gas phase for each species is given by

$$\frac{\rho_{thiol}}{\rho_{methane}} = A \times e^{\frac{\Delta H_{thiol}^{ads} - \Delta H_{methane}^{ads}}{RT}} = B \times e^{\frac{E_{thiol}^{ads} - E_{methane}^{ads}}{RT}}, \quad (16)$$

where A and B are constants of order one if the relative concentrations in the adsorbed phase are similar. We have also used the fact that the difference between isosteric heats and binding energies of adsorption are quite similar for both species [22]. It is evident that it will suffice to enhance the density of mercaptans in the adsorbed phase (relative to the desired values in the gas phase) by the reciprocal of the exponential factor in Eq. 16; i.e., if a particular concentration in the desorbed phase is desired, then the adsorbed phase must have a concentration

$$\left[\frac{\rho_{thiol}}{\rho_{methane}} \right]^{ads} = \left[\frac{\rho_{thiol}}{\rho_{methane}} \right]^{desired\ in\ gas\ phase} \times e^{\frac{E_{thiol}^{ads} - E_{methane}^{ads}}{RT}} \quad (17)$$

Considering the worst-case scenarios of adsorption energies (Table 2), to achieve the requisite 200 ppb mercaptan concentration in the gas phase, the adsorbed phase must have a mercaptan concentration of ca. 200 ppm at 298 K, and 40 ppm at 320 K. These values are modest at room temperature conditions and above. Therefore, it would be unlikely that the mercaptans presence in ANG could cause major problems contaminating or clogging the adsorbants. In consequence, the use of mercaptans/natural gas mixtures in ANG systems should be possible, without significant cost or detriment to the system performance, while maintaining a safe odorant concentration in the gas phase.

6. Summary and Conclusions

The goal of this study was to analyze the feasibility of incorporating odorant molecules in ANG systems. We focused on adsorption of gas mixtures in semi-finite, 0.7 nm wide pores in a wide range of pressures and temperatures of 195 K, 298 K and 320 K. The geometry of the pore was chosen to model the extreme situation, with strongest adsorption potentials (due to the superposition of the van der Waals contributions from both pore walls) and molecular motion that is strongly hindered (steric constraints in narrow pores). We believe that this geometry represents the most irreversible conditions for the adsorption, in particular of mercaptans, due to their strength of binding to the substrate.

Our analysis shows that even in constrained geometries the adsorption of methane and odorant molecules remains reversible. Methyl mercaptan is able to migrate within the pore volume, desorb and/or migrate between pores. Even though mercaptans bind to the adsorbent's surface more strongly than methane, only a relatively modest increase of mercaptan concentration in the adsorbed phase is necessary to keep its concentration in the gas phase above human detection threshold. The estimated concentration levels in the adsorbed phase are in the parts per million (vs. parts per billion in the gas phase). It appears to be unlikely that at suggested odorants' concentrations pore clogging would be significant. From this perspective, a safe ANG

tank should be able to operate continuously for numerous charge-discharge (adsorption-desorption) cycles before any additional processing is needed (such as moderate heating of the ANG tank while connected to a vacuum pump). Our studies show that odorant molecules can be used in ANG systems for enhanced security without major increase in cost and without adsorbent poisoning.

References

- [1] United States Federal Register 49 CFR 192.625(a), Canadian Standards Organization Z662-99 Sect. 4.17.1
- [2] Albesa A G, Llanos J L and Vicente J 2009 Comparative Study of Methane Adsorption on Graphite *Langmuir* **24** 3836-40
- [3] Ayappa K G and Ghatak C 2002 The structure of frozen phases in slit nanopores: A grand canonical Monte Carlo study *J. Chem. Phys.* **117** 5373-83
- [4] Bashkova S, Bagreev A and Bandosz T J 2002 Effect of Surface Characteristics on Adsorption of Methyl Mercaptan on Activated Carbons *Ind. Eng. Chem. Res.* **41** 4346-52
- [5] Bhatia S K and Myers A L 2006 Optimum Conditions for Adsorptive Storage *Langmuir* **22** 1688-700
- [6] Dai X D, Liu X M, Qian L, Qiao K and Yan Z F 2008 Pilot Preparation of Activated Carbon for Natural Gas Storage *Energy Fuels* **22** 3420-3
- [7] Davies G M and Seaton N A 1998 The effect of the choice of pore model on the characterization of the internal structure of microporous carbons using pore size distribution *Carbon* **36** 1473-90
- [8] Do D D and Do H D 2005 Evaluation of 1-Site and 5-Site Models of Methane on Its Adsorption on Graphite and in Graphitic Slit Pores *J. Phys. Chem. B* **109** 19288-95
- [9] El-Sheikha S M, Barakat K and Salem N M 2006 Phase transitions of methane using molecular dynamics simulations *J. Chem. Phys.* **124**
- [10] Gusev V Y and O'Brien J A 1997 A Self-Consistent Method for Characterization of Activated Carbons Using Supercritical Adsorption and Grand Canonical Monte Carlo Simulations *Langmuir* **13** 2815-21
- [11] He Y and Seaton N A 2005 Monte Carlo Simulation and Pore-Size Distribution Analysis of the Isothermic Heat of Adsorption of Methane in Activated Carbon *Langmuir* **21** 8297-301
- [12] Jorgensen W L 1998 *OPLS Force Fields*. vol 3 (New York: Wiley)
- [13] MacKerell J, A.D., Brooks B, Brooks I, C.B. , Nilsson L, Roux B, Won Y and Karplus M 1998 *CHARMM: The Energy Function and Its Parametrization with an Overview of the Program* vol 1 (Chichester: Wiley & sons)
- [14] Martin M G and Siepmann J I 1998 Transferable Potentials for Phase Equilibria. 1. United-Atom Description of n-Alkanes *J. Phys. Chem. B* **102** 2469-577
- [15] Matrangola K R, Myers A L and Glandt E D 1992 Storage of natural gas by adsorption on activated carbon *Chemical Engineering Science* **47** 1569-79
- [16] Nguyen T X, Bhatia S K and Nicholson D 2002 Close packed transitions in slit-shaped pores: Density functional theory study of methane adsorption capacity in carbon *J. Chem. Phys.* **11** 10827-36
- [17] Nicholson D 1998 Simulation studies of methane transport in model graphite micropores *Carbon* **36** 1511-23

- [18] Pfeifer P, Burress J W, Wood M B, Lapilli C M, Barker S A, Pobst J S, Cepel R J, Wexler C, Shah P S, Gordon M J, Suppes G J, Buckley S P, Radke D J, Ilavsky J, Dillon A C, Parilla P A, Benham M, Roth M W and Savage N 2008 High-Surface-Area Biocarbons for Reversible On-Board Storage of Natural Gas and Hydrogen *Mater. Res. Soc. Symp. Proc.* **1041** 1041-R02-02
- [19] Phillips J C, Braun R, Wang W, Gumbart J, Tajkhorshid E, Villa E, Chipot C, Skeel R D, Kale L and Schulten K 2005 Scalable Molecular Dynamics with NAMD *J. Comput. Chem.* **26** 1781-802
- [20] Ravikovitch P I, Vishnyakov A, Russo R and Neimark A V 2000 Unified Approach to Pore Size Characterization of Microporous Carbonaceous Materials from N₂, Ar, and CO₂ Adsorption Isotherms *Langmuir* **16** 2311-20
- [21] Schlick T 2006 *Molecular modeling and simulation: An interdisciplinary guide* vol 21 (New York: Springer Science+Business Media, LLC)
- [22] Sircar S, Mohr R, Ristic C and Rao M B 1999 Isosteric Heat of Adsorption: Theory and Experiment *J. Phys. Chem. B* **103**
- [23] Sweatman M B and Quirke N 2001 Characterization of Porous Materials by Gas Adsorption at Ambient Temperatures and High Pressure *J. Phys. Chem. B* **105** 1403-11
- [24] Sweatman M B and Quirke N 2005 Gas Adsorption in Active Carbons and the Slit-Pore Model 1: Pure Gas Adsorption *J. Phys. Chem. B* **109** 10381-8
- [25] Tafipolsky M, Amirjalayer S and Schmid R 2009 Atomistic theoretical models for nanoporous hybrid materials *Microporous and Mesoporous Materials* **124** 110–6
- [26] Wark and Kenneth (1988) [1966] *Generalized Thermodynamic Relationships*. (New York, NY: McGraw-Hill, Inc.)